# Inverse Design of Spectrally-Selective Films for PbS-CQD Tandem Solar Cells

Sreyas Chintapalli, Tina Gao, Luna Singh, Serene Kamal, Arlene Chiu, Yijun Zhang, Susanna M. Thon

Johns Hopkins University, Baltimore, MD 21218 USA

Abstract — We present a method for designing spectrally-selective optoelectronic films with a finite absorption bandwidth. We demonstrate the process by designing a film composed of lead sulfide colloidal quantum dots (PbS-CQDs). Designs incorporate the patterning of absorbing PbS-CQD films into photonic crystal-like slabs which couple incident light into leaky modes within the plane of the absorbing films, modulating the absorption spectrum. Computational times required to calculate optical spectra are drastically decreased by implementing the Fourier Modal Method. Furthermore, a supervised machine-learning-based inverse design methodology is presented which allows tailoring of the PbS-CQD film optical properties for use in a variety of photovoltaic applications, such as tandem cells in which spectral tailoring can enable current-matching flexilibility.

#### I. INTRODUCTION

Tandem solar cells (TSC) are an area of large interest to their demonstrated potential to increase solar cell efficiencies beyond current efficiency limits [1]-[2]. In the typical TSC architecture, the ultraviolet-visible cell (VIS Cell) is placed above the infrared absorbing cell (IR cell), closer to the incident illumination. This maximizes photoconversion efficiency by preventing thermalization loss from occurring in the infrared cell, as high energy photons are absorbed prior to exciting charge carriers in the bottom IR cell [3]. Lead sulfide colloidal quantum dots (PbS-CQDs) have a size-tunable bandgap due to quantum confinement, which makes them a promising candidate for use in tandem solar cells as an IR absorber. However, PbS-CQDs, as well as other candidate IR absorbing materials, are unstable at temperatures even as high as 120°C [4]. This places significant processing constraints on device architectures incorporating these films, because after the CQD film is deposited, any further high-temperature processing will degrade device performance. This effectively restricts all layers on top of the IR cell be processed at relatively low temperatures.

Tandem device architectures where the IR cell could be placed on top of existing VIS architectures would provide great flexibility in both material choice for other layers, as well as the ability to quickly leverage existing high efficiency designs for VIS single junction solar cells. To mitigate the thermalization loss, the PbS-CQD film would need to have suppressed absorption in the absorption range of the VIS cell. While all semiconductor-like (SC-like) materials have absorption that continues above some threshold energy, in this

work we propose to pattern PbS-CQD films using a photonic crystal-like slab (PhC) structure. In our earlier work, we have shown that patterning PbS-CQD films can modulate their absorption spectra [5]. In this work, we propose a method for designing and patterning films with a finite absorption bandwidth (FAB) which give the desired absorption properties in the IR, as well as desired transmission in the visible spectral range, through incident light coupling into leaky guided modes in the patterned film. This allows for using existing materials and patterning techniques to create custom optical absorption behavior, which can be optimized for many tandem device architectures.

#### II. METHODOLOGY

### A. PbS-CQD Film Characterization

PbS-CQD films were synthesized using the hot-injection method [8], with various target exciton peak wavelengths. The films were measured using a J.A. Woollam UV-NIR Variable Angle Spectroscopic Ellispometer (VASE) to extract refractive index models. The real and imaginary components are shown in Fig. 1(a) and (b) respectively, with the physical quantum dot sizes calculated from [6] shown in the legend. This model was chosen because it corresponds to  $E_g \approx 1.05$  eV, close to the ideal bandgap for a tandem IR cell [9].

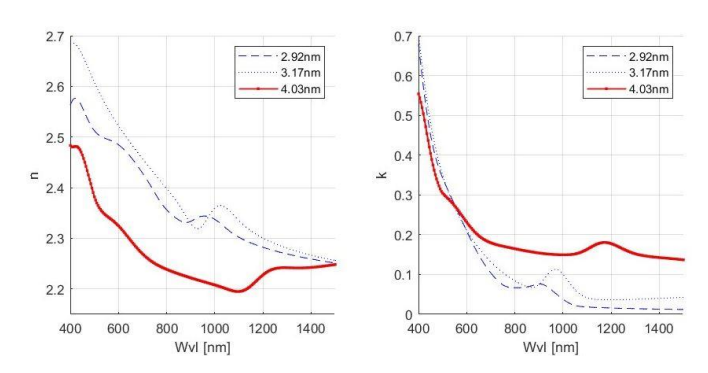


Fig. 1 (a) Real component of refractive index of PbS-CQD Films. (b) Extinction coefficient of PbS-CQD Films. The values in the legend correspond to estimated CQD diameters. The red index model is the model used for the remainder of this work.

In our previous work, we showed that the out-of-plane transmission and reflection spectra of the patterned films couple strongly to in-plane guided modes, even in the presence of absorption [6]. Here, we generate spectra directly from traditional designs We chose a spectral range of 400-1500 nm for the assumed incident light. The design parameters were searched within the following bounds: lattice constant, a, from 100-1500 nm; normalized feature radius, r/a, from 0.05 to 0.5; and normalized slab thickness, t/a, from 0.1 to 2.1. The figure-of-merit (FOM) is given in Equation 1, where w is the weight given to the visible portion of the spectrum during optimization,  $T_{vis}$  is the transmission spectrum,  $A_{IR}$  is the absorption spectrum, and  $\lambda$  is the wavelength of incidence.

$$FOM = \max\left(w \int T_{VIS}(\lambda) \ d\lambda + (1 - w) \int A_{IR}(\lambda) \ d\lambda\right) (1)$$

This FOM allows us to balance the two design goals between keeping absorbance high in the IR, while allowing the PbS-CQD absorbing film to transmit light to the VIS cell below. Both terms are needed, as the globally optimal solutoin for either the first or second term individually would lead to the thinnest or thickest possible film, respectively. Figure 2(a) shows the absorption and transmission spectra of a hexagonal-hole film compared to an equivalent film with the same volume of PbS-CQD. The shaded region highlights Eg>1.65eV, the

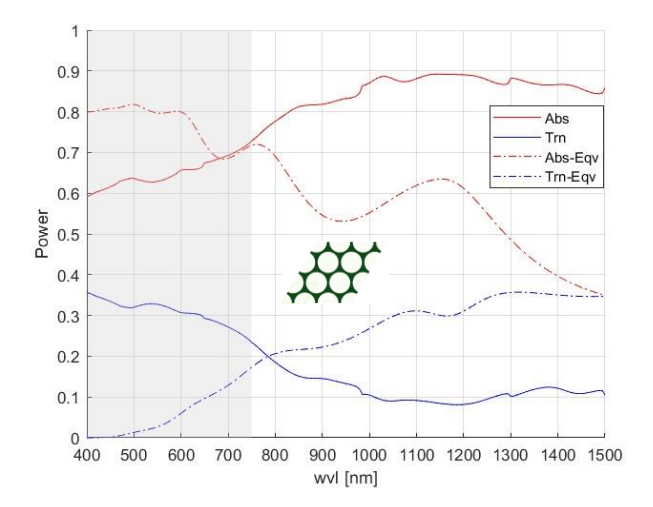


Fig. 2. Optical Spectra of a patterned and unpatterned PbS-CQD film. Red lines are absorption spectra, and blue are transmission spectra. Dashed lines represent the equivalent unpatterned film. The film has a lattice constant of 1500nm, normalized radius of 0.45(675nm), and normalized thickness of 1.3 (1950nm). A few unit cells of the pattern are shown in the center inset, with green representing PbS-CQDs and white representing air.

optimal bandgap for the corresponding VIS cell [8]. With even this simple design, there is a 23.7% increase in the transmission across the visible range, and 10.9% suppression of the absorption.

Machine learning techniques for the inverse design of metasurfaces and other optical structures have gained prominence in recent year, as these models have the ability to generate high performance, but unintuitive designs [9]-[10]. We use a network architecture inspired by the model used in [11]-[12]. Our model is a multi-input multi-output model that fully parametrizes the design of the patterned film needed for a desired spectrum. Three classes of shapes were used for masks: Bezier polygons, reflectively symmetric, and radially, along with a random scalar lattice constant and thickness, using the same Nannos implementation as the previous section [7]. Spectra were generated for all 30,000 mask-spectra pairs for at 5nm wavelength spacing across 400-1500nm. These spectra were split into proportions of 70%, 20%, and 10% for the training, validation, and testing sets. The entire network, implemented in TensorFlow is available at online at [13], and the random splits are seeded for reproducibility, along with the detailed diagram of the model architecture. The encoder takes each mask and encodes this into a linear 128 dimension feature space similar to [11]. This feature vector concatenates directly with the 2 lattice parameters. The model then goes through a series of fully-connected layers and recovers 665 parameters. The first 663 correspond to each optical spectra (of length 221 each), and the last two elements are the estimators of the recovered lattice parameters. Figure 3 shows examples of the encoding/prediction process. We used the ADAM optimizer [14] with the standard learning rate of 0.001 to minimize the mean-squared error. The process is then reversed and the mask is regenerated from the feature space.

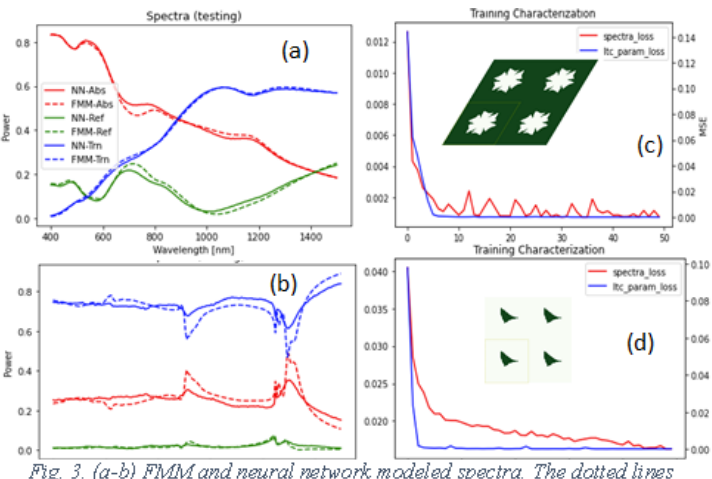


Fig. 3. (a-b) FMM and neural network modeled spectra. The dotted lines represent the FMM model, and the solid lines are the predictions of the encoder. Lattice parameters of (a) were  $(a,t_a)=(1250,0.7)$  with a prediction of (1283, 0.66). Lattice parameters of (b) were  $(a,t_a)=(1250,0.7)$  with a prediction of (1283, 0.66).

(c-d) Training characterization of the model trained on the two lattice types pictures. (a) corresponds to (c) and (b) corresponds to (d). The unit cells passed to the encoder were in the test set, and never seen by the model.

#### III. DISCUSSION

The tuning of the weights for the loss was critical in the neural network. We use the loss as 0.25 for the spectral encoding, and 0.75 for the lattice parameters Fig 3(a), and as we ed that the mask shape will have a more nuanced effect, as the lattice parameters will strongly define coupling of the incident light leaky modes (in-plane of the crystal as well as the Fabry-Perot modes from the slab thickness). The model is very lightweight, training in less than 6 minutes using the free Google Colab platform, using a batch size of 50 samples over 50 epochs. While the encoding process has relatively high accuracy, and can be further improved with hyperparameter tuning, or drastically increasing the number of variables (and therefore training time), we note that the error from our 'ideal spectrum' for a top IR PbS-CQD absorbing layer is quite high. Unfortunately, it is difficult, if not impossible, to calculate the theoretical minimum of how close one can get to an arbitrary spectrum do to the nearly infinite search space of possible unit cells, but given the constraints of the real index models. As one can see, the 'rod-square' lattice pattern in Fig. 3(d) allows nearly 80% transparency everywhere below the exciton peak of 1200nm of the PbS-CQDs. Here we have used the exact same model on each of the lattice types, which is convenient, but may not be the highest performance. Additionally, we use the exact same features during the encoding and decoding process, which also may not yield the maximum possible FOM.

#### IV. SUMMARY AND OUTLOOK

We have demonstrated a method to improve manufacturing flexibility of tandem cells using PbS-CQDs, as well as the possibility to design custom films to leverage existing VIS cells. In order to further improve these models, as well as realize them in tandem cells, the models can be tuned through various hyperparameter optimizations as well as have enforced manufacturability constraints. The size scale of the unit cells of the inversely designed films are ~600nm, which is within the feature scale of nanoimprint lithography techniques [14] for quantum dots. These methods are also flexible enough that the optical properties of underlying films/substrates can be readily added, due to the flexibility of

## V. ACKNOWLEDGEMENTS

We would like to acknowledge the National Science Foundation (ECCS-1846239) for funding this work. This work was carried out at the Advanced Research Computing at Hopkins (ARCH) core facility (rockfish.jhu.edu), which is supported by National Science Foundation (NSF) grant number OAC1920103.

#### REFERENCES

- [1] T. Ameri, G. Dennler, C. Lungenschmied, and C. J. Brabec, "Organic tandem solar cells: A review," *Energy Environ. Sci.*, vol. 2, no. 4, p. 347, 2009, doi: 10.1039/b817952b.
- [2] A. D. Vos, "Detailed balance limit of the efficiency of tandem solar cells," *J. Phys. D: Appl. Phys.*, vol. 13, no. 5, pp. 839–846, May 1980, doi: 10.1088/0022-3727/13/5/018.
- [3] T. Todorov, O. Gunawan, and S. Guha, "A road towards 25% efficiency and beyond: perovskite tandem solar cells," *Mol. Syst. Des. Eng.*, vol. 1, no. 4, pp. 370–376, 2016, doi: 10.1039/C6ME00041J.
- [4] M. Albaladejo Siguan, E. C. Baird, D. Becker Koch, Y. Li, A. L. Rogach, and Y. Vaynzof, "Stability of Quantum Dot Solar Cells: A Matter of (Life)Time," *Adv. Energy Mater.*, vol. 11, no. 12, p. 2003457, Mar. 2021, doi: 10.1002/aenm.202003457
- [5] B. Qiu, Y. Lin, E. S. Arinze, A. Chiu, L. Li, and S. M. Thon, "Photonic band engineering in absorbing media for spectrally selective optoelectronic films," *Opt. Express,* vol. 26, no. 21, p. 26933, Oct. 2018, doi: 10.1364/OE.26.026933.
- [6] I. Moreels et al., "Size-Dependent Optical Properties of Colloidal PbS Quantum Dots," *ACS Nano*, vol. 3, no. 10, pp. 3023–3030, Oct. 2009, doi: 10.1021/nn900863a.
- [7] B. Vial and Y. Hao, "Open-Source Computational Photonics with Auto Differentiable Topology Optimization," *Mathematics*, vol. 10, no. 20, p. 3912, Oct. 2022, doi: 10.3390/math10203912.
- [8] T. Leijtens, K. A. Bush, R. Prasanna, and M. D. McGehee, "Opportunities and challenges for tandem solar cells using metal halide perovskite semiconductors," *Nat Energy*, vol. 3, no. 10, pp. 828–838, Jul. 2018, doi: 10.1038/s41560-018-0190-4.
- [9] S. Molesky, Z. Lin, A. Y. Piggott, W. Jin, J. Vucković, and A. W. Rodriguez, "Inverse design in nanophotonics," *Nature Photon*, vol. 12, no. 11, pp. 659–670, Nov. 2018, doi: 10.1038/s41566-018-0246-9.
- [10] P. R. Wiecha, A. Arbouet, C. Girard, and O. L. Muskens, "Deep learning in nano-photonics: inverse design and beyond," *Photon. Res.*, vol. 9, no. 5, p. B182, May 2021, doi: 10.1364/PRJ.415960.
- [11] T. Christensen et al., "Predictive and generative machine learning models for photonic crystals," *Nanophotonics*, vol. 9, no. 13, pp. 4183–4192, Jun. 2020, doi: 10.1515/nanoph-2020-0197.
- [12] A. Nikulin, I. Zisman, M. Eich, A. Yu. Petrov, and A. Itin, "Machine learning models for photonic crystals band diagram prediction and gap optimisation," *Photonics and Nanostructures Fundamentals and Applications*, vol. 52, p. 101076, Dec. 2022, doi: 10.1016/j.photonics.2022.101076.
- [13]. Chintapalli, I (2023). Shaped-PbS-CNN. (Version 1. 1). https://github.com/jhu-nanoenergy/spectral\_selectivity
- [14] M. J. Hampton, J. L. Templeton, and J. M. DeSimone, "Direct Patterning of CdSe Quantum Dots into Sub-100 nm Structures," *Langmuir*, vol. 26, no. 5, pp. 3012–3015, Mar. 2010, doi: 10.1021/la904787k.